Electronic Supplementary Material (ESI) for Energy & Environmental Science.
This journal is © The Royal Society of Chemistry 2024

Supporting Information

High Performance Eco-friendly MgAgSb-Based Thermoelectric Power Generation Device Near Phase Transition Temperatures

Xinzhi Wu[1,†], Yangjian Lin[2,†], Chengyan Liu[1,†], Yupeng Wang[1], Huan Li[1], Binghui Ge[*,2], Weishu Liu*[,1,3]

1. Department of Materials Science and Engineering, Southern University of Science and Technology, Shenzhen, Guangdong 518055, China
2. Information Materials and Intelligent Sensing Laboratory of Anhui Province, Institutes of Physical Science and Information Technology, Anhui University, Hefei, Anhui 230601, China
3. Guangdong Provincial Key Laboratory of Functional Oxide Materials and Devices, Southern University of Science and Technology, Shenzhen, Guangdong 518055, China

† Equally contributed,

* Corresponding Author: liuws@sustech.edu.cn, and Bhge@ahu.edu.cn

1. Experiments

1.1 Preparation

The nominal composition of the TEcM was p-type $MgAg_{0.97}Sb_{0.92}$ (abbreviated as MgAgSb) and n-type $Mg_{3.2}Sb_{1.5}Bi_{0.49}Te_{0.01}Ti_{0.01}$ (abbreviated as $Mg_3Sb_{1.5}Bi_{0.5}$), synthesized via mechanical alloying (MA, SPEX 800D) and spark plasma sintering (SPS, 211Lx, Fuji Electronic Industrial Co. Ltd.). The TEiMs powders were generated via ball milling and then merged onto the TEcM powder via SPS to form the TEiM/TEcM contact interfaces. Detailed preparation of the MgAgSb [1], $Mg_3Sb_{1.5}Bi_{0.5}$ TEcM [2], TEiM/TEcM contact interfaces [3], and TE device [4] can be found in our previous studies.

The single-leg TE devices (approximately $4 \times 4 \times 8$ mm^3) are composed of MgAgSb TEcM and $AgMgMn_{0.1}$ TEiM, and the thicknesses of the MgAgSb and $AgMgMn_{0.1}$ layers were designed to be approximately 6 and 1 mm, respectively. The two-couple MgAgSb-$Mg_3Sb_{1.5}Bi_{0.5}$ TE module with dimensions of 10 × 10 × 10 mm^3 was assembled by sintered silver paste LTAg (Fanyada Electronic Technology Co., Ltd.). The assembly process is kept at 175 °C in the vacuum for 150 min.

1.2 Characterization

The Seebeck coefficient (S) and electrical resistivity (ρ) were obtained using a commercial system (CTA, Cryoall). Thermal diffusivity (D) was determined using a laser flash method (LFA467, Netzsch). Thermal conductivity (κ) was computed using the formula $\kappa=D\times d\times C_p$, where the density ($d$) and specific heat capacity (C_p) were obtained employing an Archimedes method and a differential scanning calorimeter (DSC Discovery, Waters LLC), respectively. The power factor (PF) and dimensionless figure-of-merit (ZT) could be computed by the formula $PF=S^2/\rho$, and $ZT=PF/\kappa T$, respectively. The coefficient of thermal expansion (α) was measured using a Netzsch DIL instrument (TMA402, Netzsch). A universal material testing machine (68SC-1, Instron) and a custom-made probe system were utilized to determine shear strength (σ_s) and specific contact resistivity (ρ_c), respectively. The detailed test and analysis methods of σ_s and ρ_c can be seen in our previous work [3, 4].

The phase composition was characterized by X-ray diffraction (XRD, Bruker D8 Advance) with Cu K_α radiation. The microstructure and morphology were observed using scanning electron microscopy (SEM, MAIA3 TESCAN) and transmission electron microscopy (TEM). The structural characterization and in situ heating experiment were accomplished by using a JEOL-F200 and a probe-corrected JEOL NEOARM TEM operating at 200 kV and DENS solutions heating holder (chip: wildfire DS2430-W1). The in-situ TEM samples were prepared by a Carl Zeiss Crossbeam 550 FIB-SEM with a standard lift-out procedure as follows. Ion-beam-induced Pt deposition was applied inside the focus ion beam (FIB) chamber before the lift-out process. The sample was then thinned for electron transparency at the easy-lift needle and mounted onto a DENS solutions heating chip, where the target area was further polished several times to a specific TEM sample thickness. After that, the sample was loaded into a microscope for the in-situ heating experiment at once.

The performance of the device was obtained with custom-made equipment [4]. The terminal voltage (V), and output power (P) were measured by changing the current (I) under different hot side temperatures (T_h). The T_h was set as 100–330 °C, while the cold-side temperature (T_c) was fixed at approximately 5 °C. The conversion efficiency (η) and power density (ω) were then computed using the formulas, $\eta = \frac{P}{Q_h} = \frac{V \times I}{V \times I + Q_c}$, and $\omega = \frac{P}{A_{Device}} \times 100\%$, respectively. The cold side heat flow (Q_c) was evaluated by the one-dimensional Fourier's law, $Q_c = \frac{\kappa A}{L} \Delta T$ where κ, A, L, and ΔT are the thermal conductivity, cross-section area (4×4 mm^2 and 10×10 mm^2 for single-leg and 2-pair module, respectively), thermocouple spacing length, and temperature difference of the heat flow meter (Brass 82 W m^{-1} K^{-1}). The performance of TE devices was simulated employing a finite element method. A steady-state temperature gradient is applied to the cold and hot sides with a mechanical boundary for thermal stress assess. The T_c was fixed at 5 °C, and the T_h increased from 100 to 330 °C for TE power generation, while ΔT-dependent coefficient of performance (COP) and (maximum cooling temperature) ΔT_{max} were simulated when T_c is 27 °C and T_h increased from 37 to 97 °C, respectively for TE cooling.

2. Estimation of thermal radiation and leakage

The thermoelectric power generator is a heat engine, and the theoretical conversion efficiency (η_{theo}) is defined as $\eta_{theo} = P/Q_h$, where P and Q_h are the output power and hot side heat flow, respectively. Theoretically, the Q_h could be equal to the combination of P and the Q_c. However, from the viewpoint of engineers, there is extra heat loss due to the radiation from the hot side of samples and the heat conduction from the Cu lead (Q_{lead}) (Figure. S 21). Reference to the heat evaluation strategies [5-7], we have estimated the vertical thermal radiation ($Q_{\text{rad},\perp}$) and horizontal heat radiation ($Q_{\text{rad},//}$) during the testing progress. Besides, the heat conduction from lead on the cold side was also taken into account. A more careful calibration for the hot-side heat flow $Q_{\text{h},cali}$ is implemented, i.e., $Q_{h,cal} = P + Q_c + Q_{rad,//} - Q_{rad,\perp} - Q_{\text{lead}}$. Q_{rad} and Q_{lead} can be computed by the formula $Q_{rad} = \frac{C \times \theta \times \varepsilon}{\Delta T} \int_{T_c}^{T_h} (T^4 - T_S^4) dT$ and $Q_{lead} = \frac{\kappa_{lead} \times A_{lead}}{L_{lead}} (T_S - T_c)$, respectively, where T_s, T_h, and T_c are the environmental temperature, hot side temperature, and cold side temperature. T_h ε, θ, C are the emissivity (0.5–0.9)[8, 9], Stefan-Boltzmann constant 5.67 × 10^{-8} W m^{-2} K^{-4}, and total outside surface area, respectively. The κ_{lead}, A_{lead}, and L_{lead} are the thermal conductivity, cross-section area, and length of the lead, respectively. Finally, the calibration conversion efficiency (η_{cali}) could be defined as $\eta_{\text{cal}} = P/Q_{\text{h},cali}$, considering the theoretical thermal radiation.

3. Figure. S

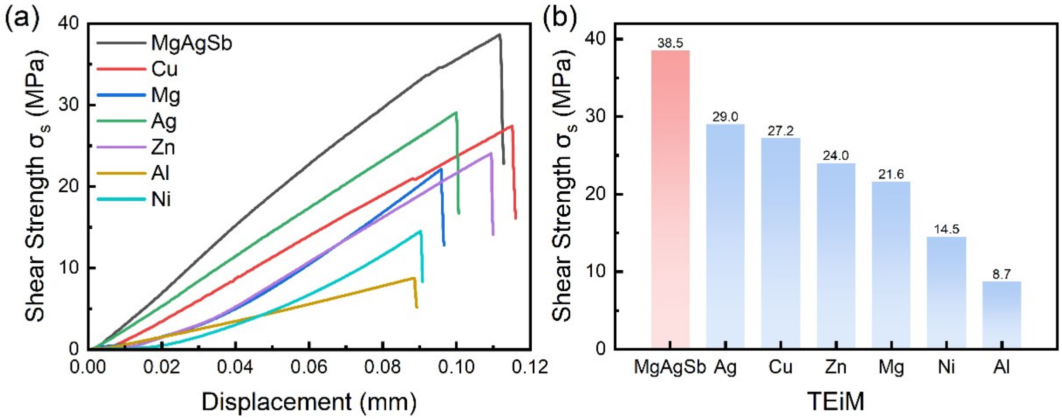

Figure. S 1 (a) Change in σ_s vs. displacement curve of the MgAgSb and TEiM/MgAgSb interfaces for estimating the σ_s, and (b) The σ_s of MgAgSb and TEiM/MgAgSb interfaces.

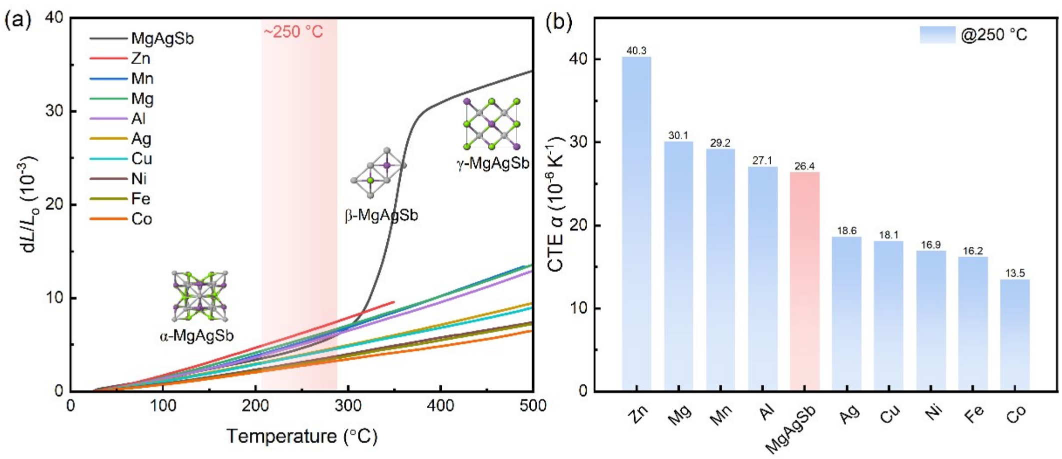

Figure. S 2 (a) and (b) are the plots of temperature-dependent strain dL/L_0 and CTE for potential pure metal and TEcM (MgAgSb), respectively.

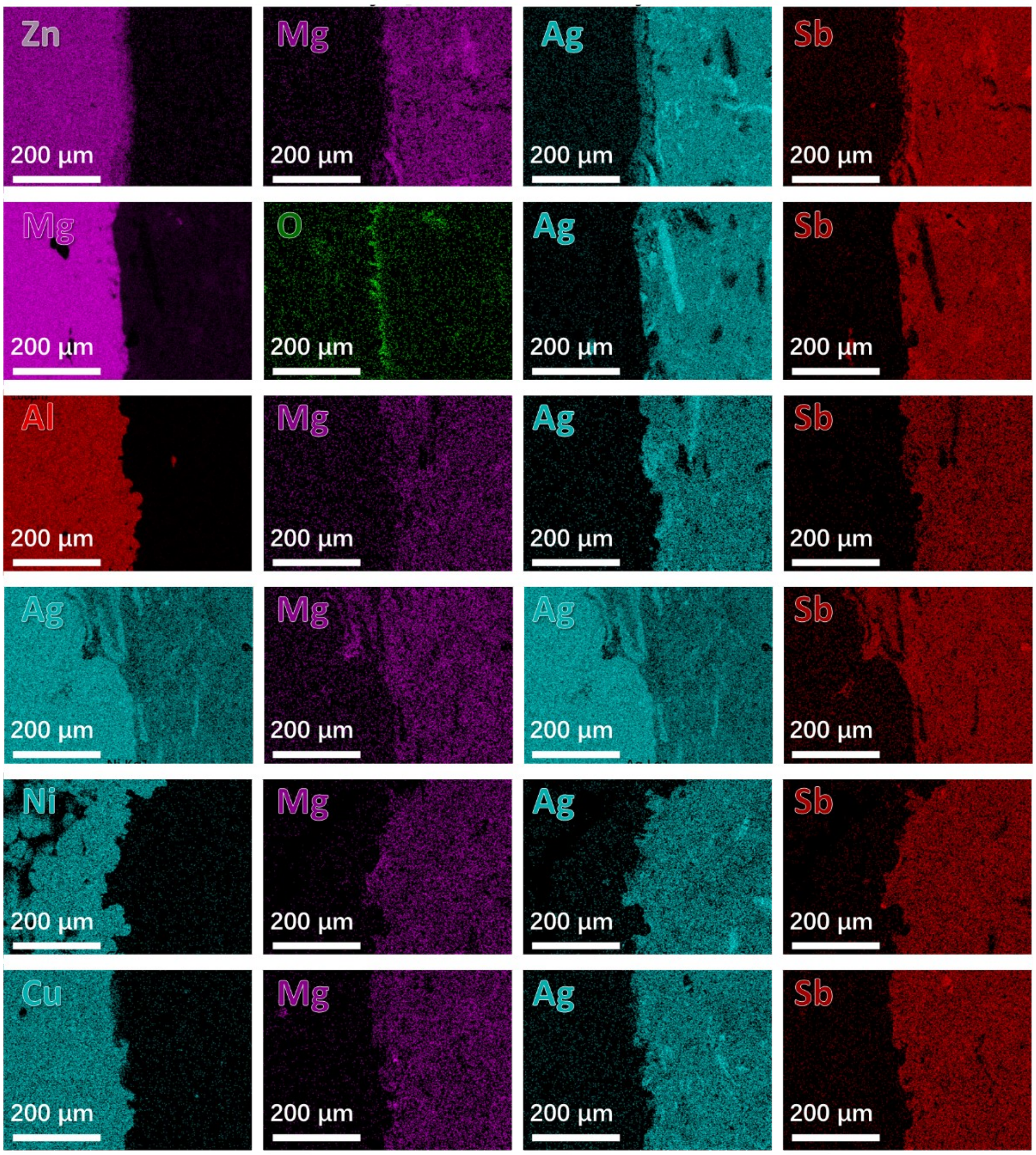

Figure. S 3 SEM images and corresponding EDS mapping of the TEiMs/MgAgSb interface.

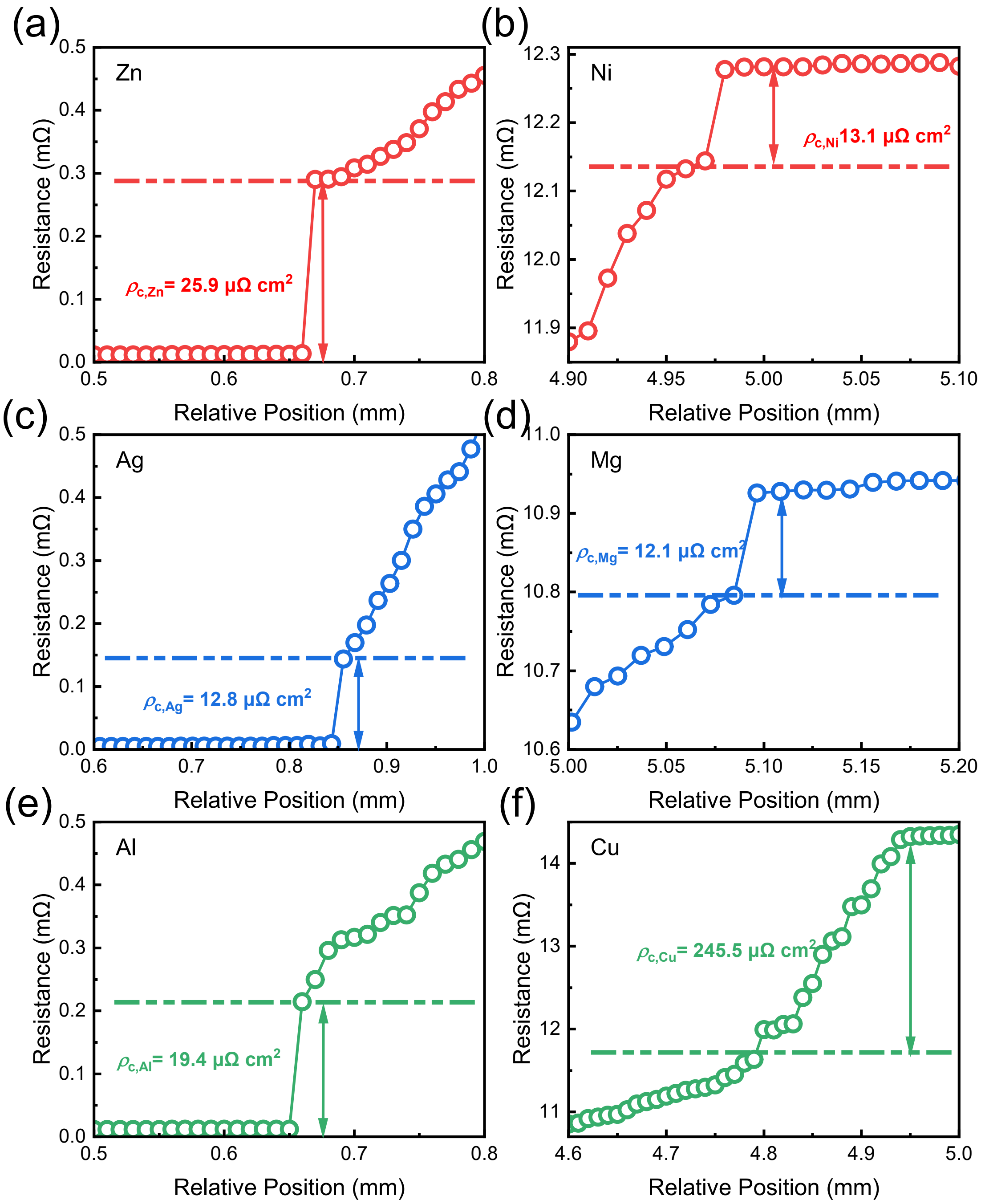

Figure. S 4 ρ_c of single element TEiM/MgAgSb interfaces. Change in resistance vs. positions curve across the TEiM/MgAgSb interfaces for estimating the ρ_c, (a) Zn/MgAgSb, (b) MgAgSb/Ni, (c) Ag/MgAgSb, (d) MgAgSb/Mg, (e) Al/MgAgSb and (f) MgAgSb/Cu.

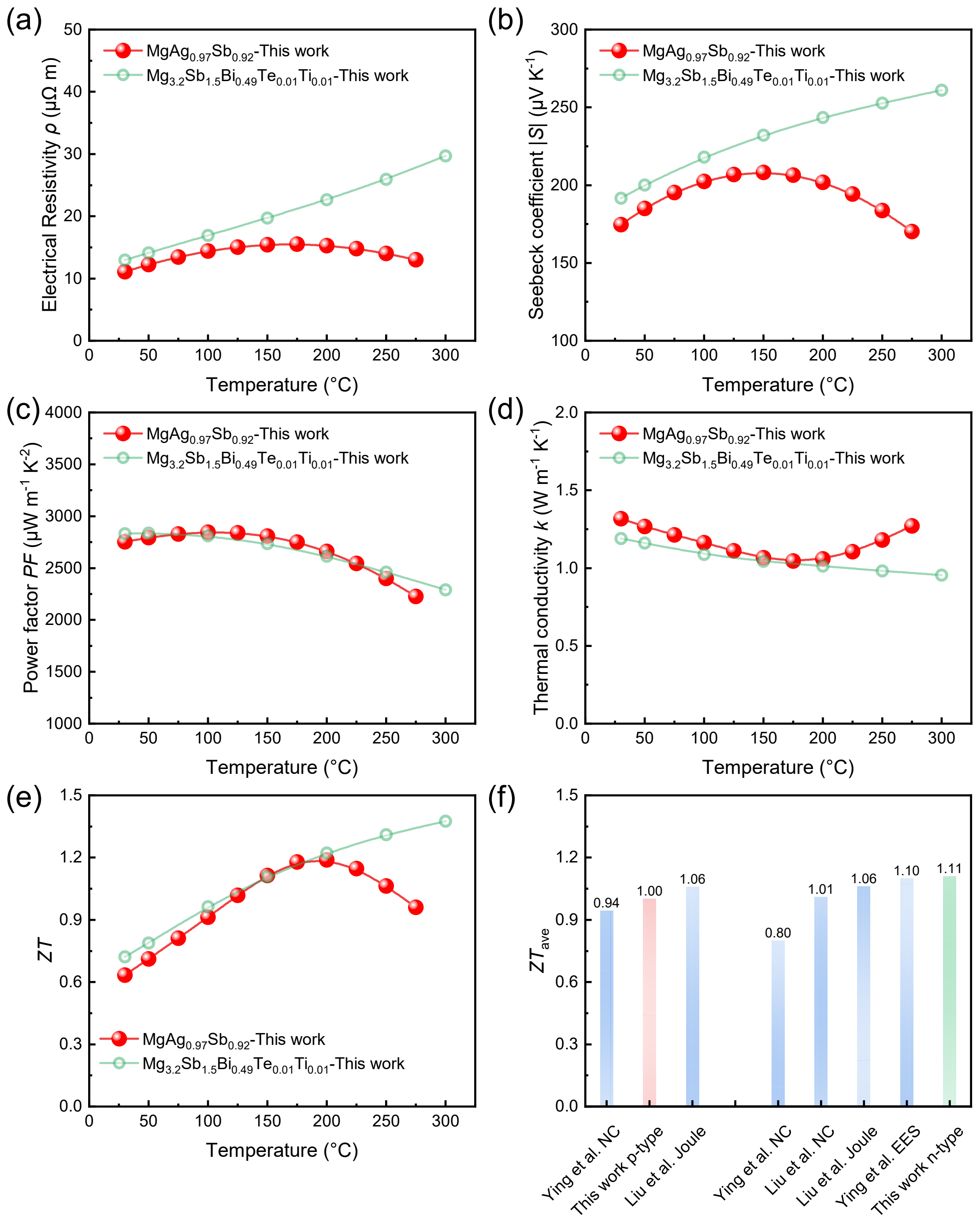

Figure. S 5 The temperature-dependent TE properties of the as-fabricated MgAgSb bulk (a) Electrical resistivity, (b) Seebeck coefficient, (c) power factor, (d) thermal conductivity, (e) ZT, and (f) ZT_{eng}. Literature results[10-13] are included for comparison.

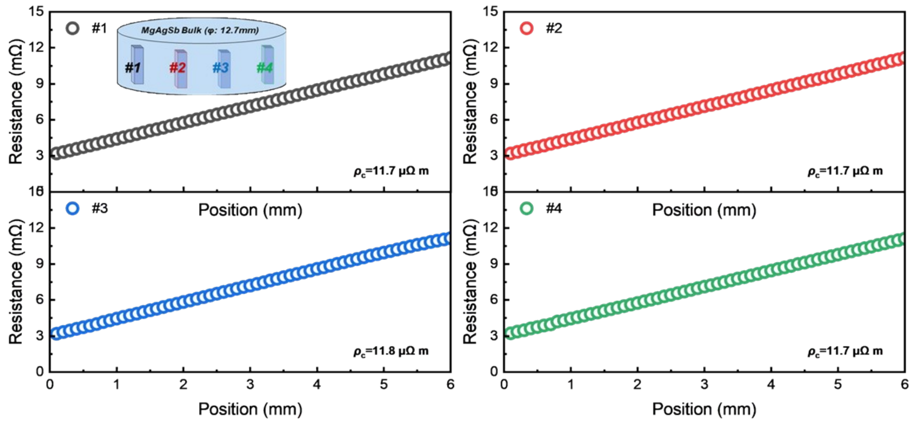

Figure. S 6 Electrical resistivity of MgAgSb at different positions measured by the home-build probe screen apparatus.

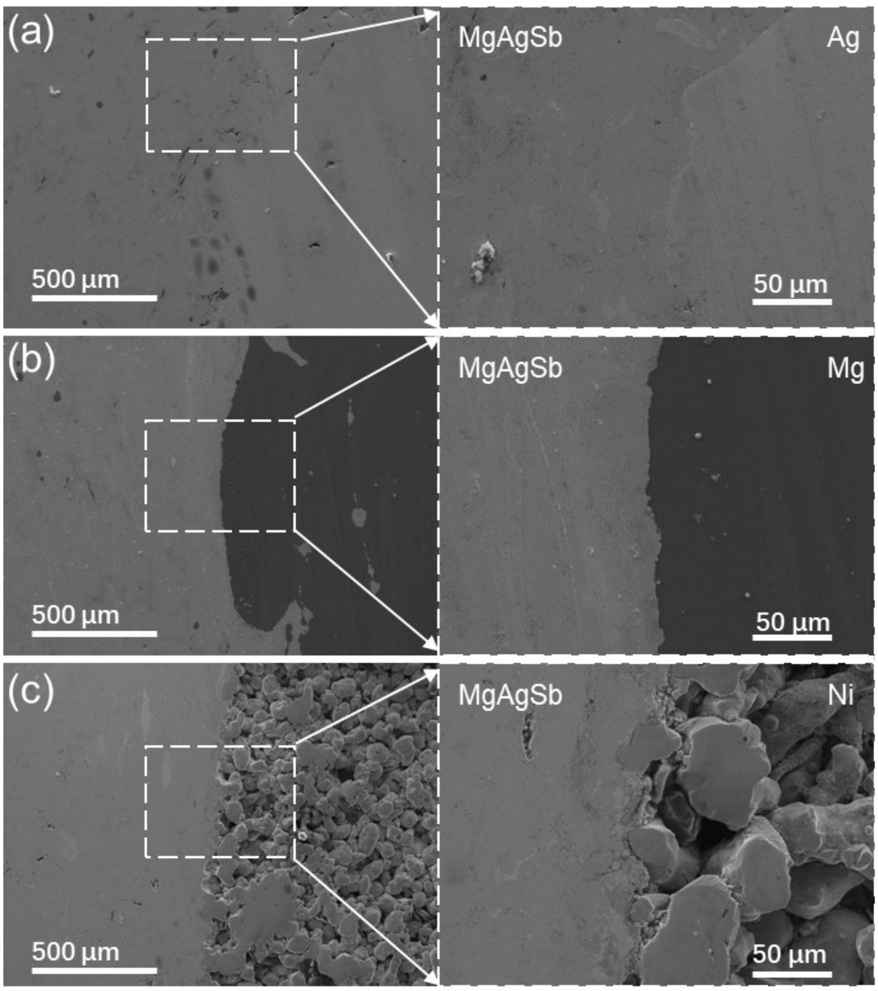

Figure. S 7 SEM images of theAg, Mg, and Ni/MgAgSb contact interface.

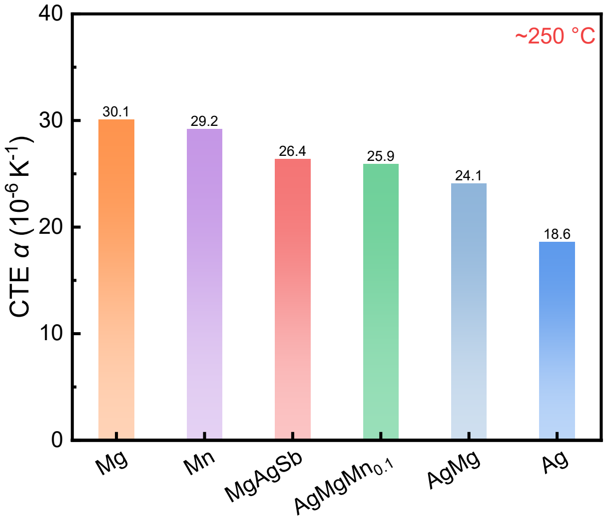

Figure. S 8 The plot CTE for potential TEiM and TEcM (MgAgSb), respectively.

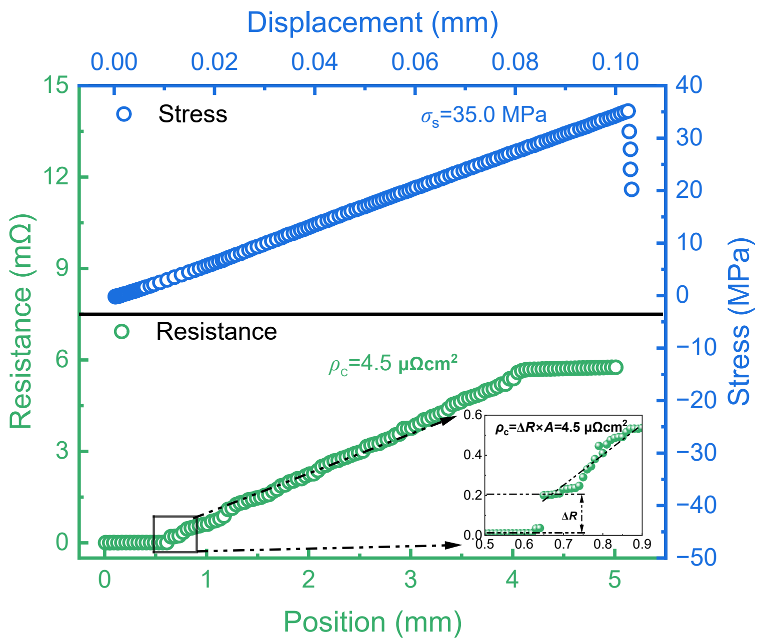

Figure. S 9 σ_s and a ρ_c of for $AgMgMn_{0.1}$/MgAgSb interface

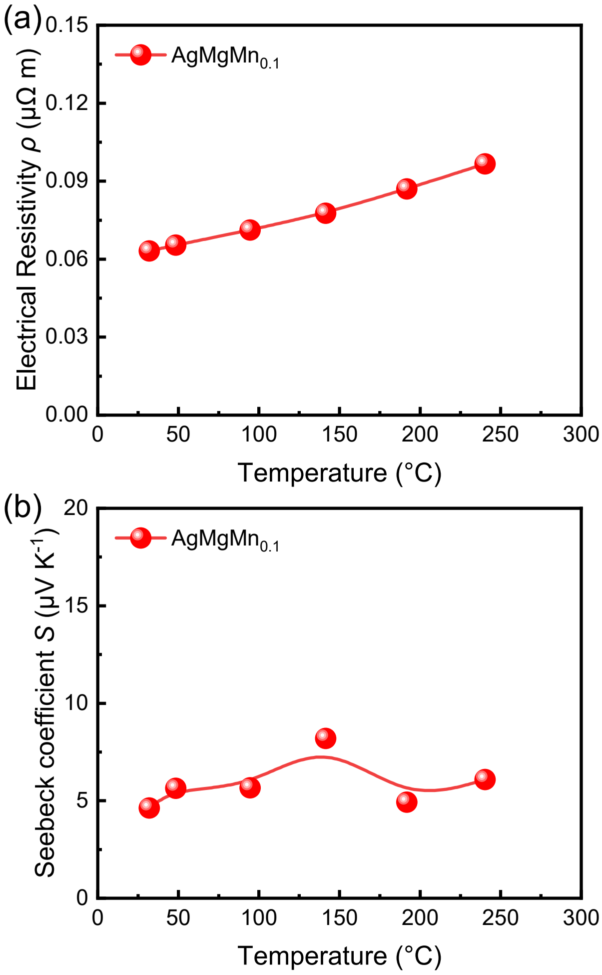

Figure. S 10 Temprature-dependent ρ (a) and S of $AgMgMn_{0.1}$

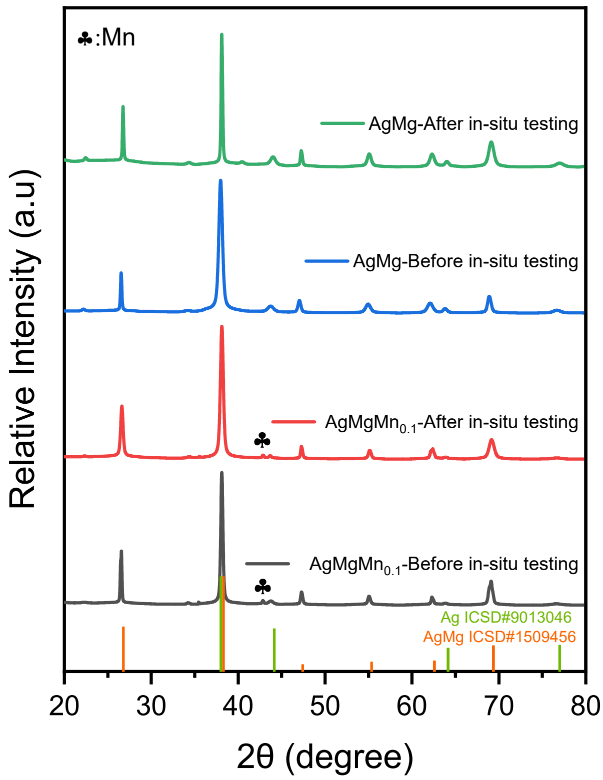

Figure. S 11 XRD patterns of MgAg and $AgMgMn_{0.1}$ before and after in situ testing at 250 °C.

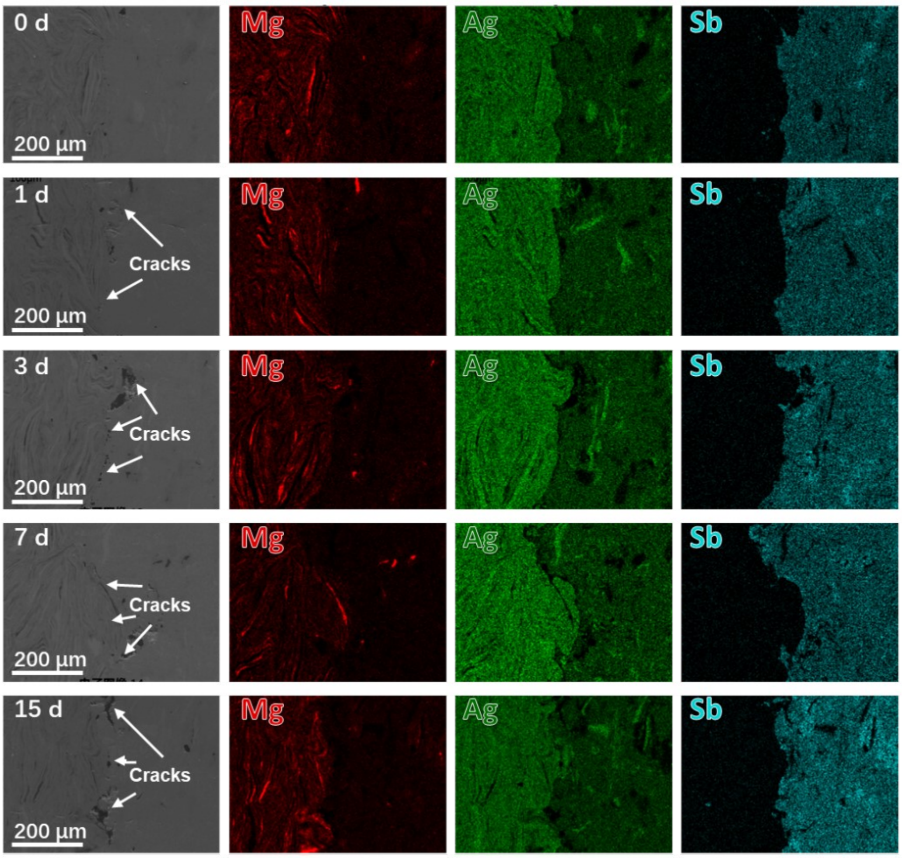

Figure. S 12 SEM images and corresponding EDS mapping of the MgAg/MgAgSb interface.

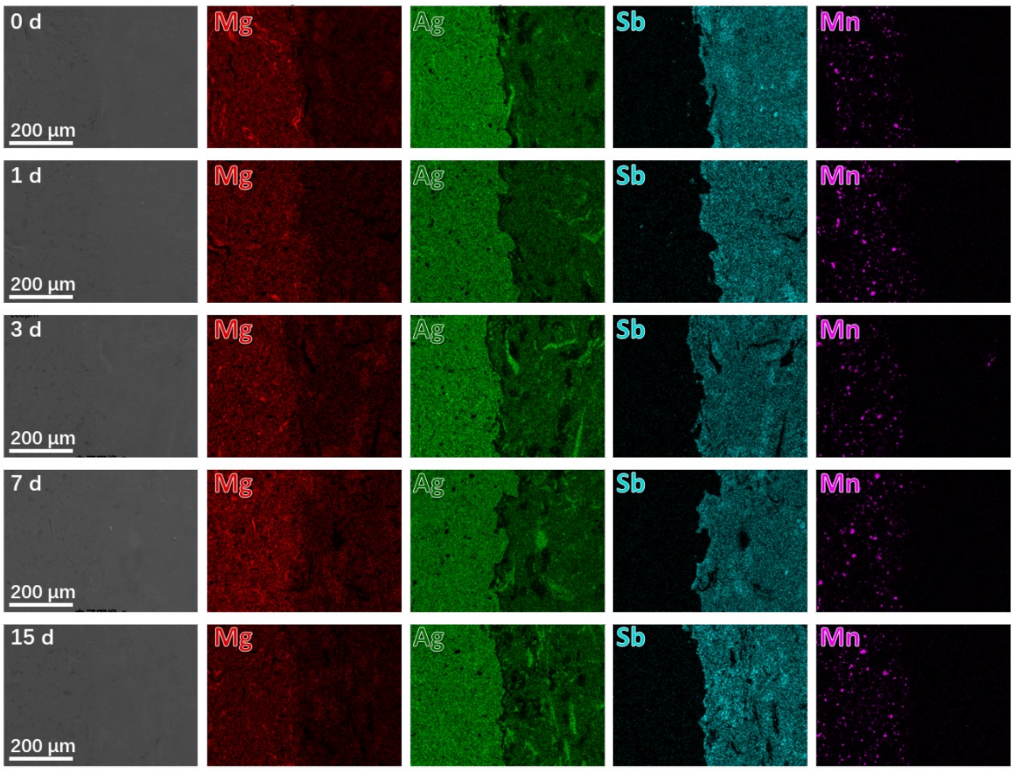

Figure. S 13 SEM images and corresponding EDS mapping of the $AgMgMn_{0.1}$/MgAgSb interface.

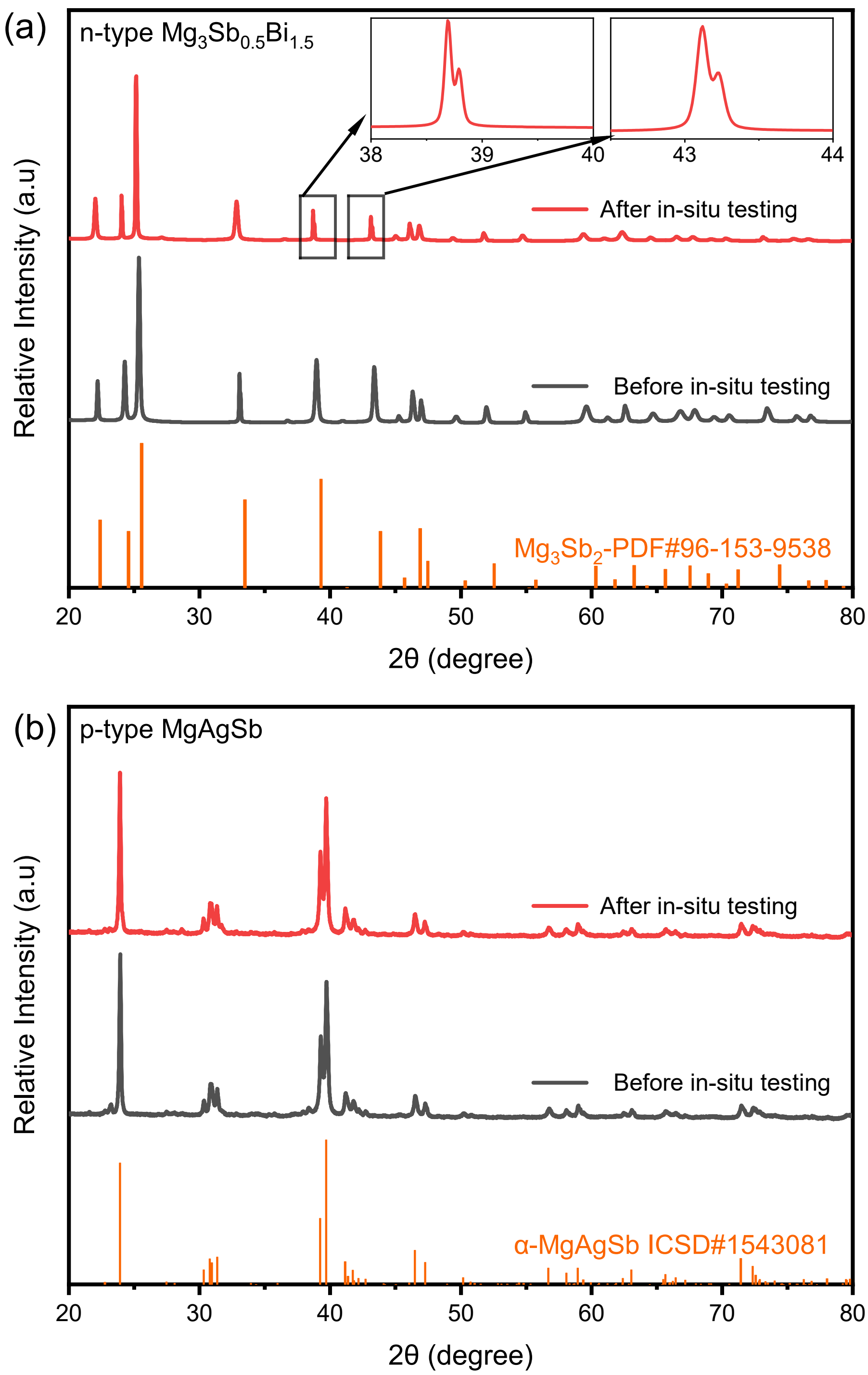

Figure. S 14 XRD patterns of the samples before and after in situ testing at 250 °C. (a) $Mg_3Sb_{1.5}Bi_{0.5}$, (b) MgAgSb

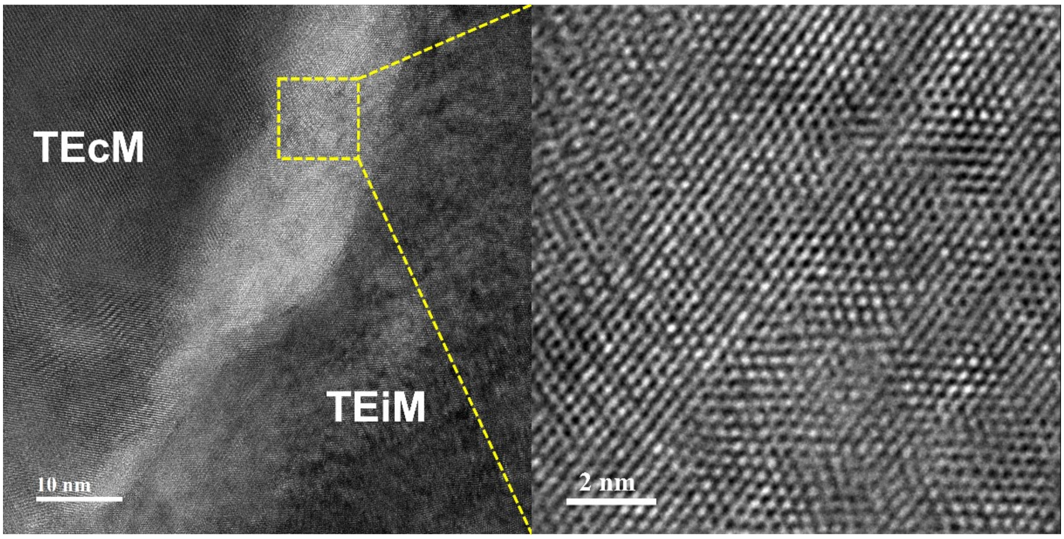

Figure. S 15 HRTEM images of the $AgMgMn_{0.1}$/MgAgSb interface under 250 °C.

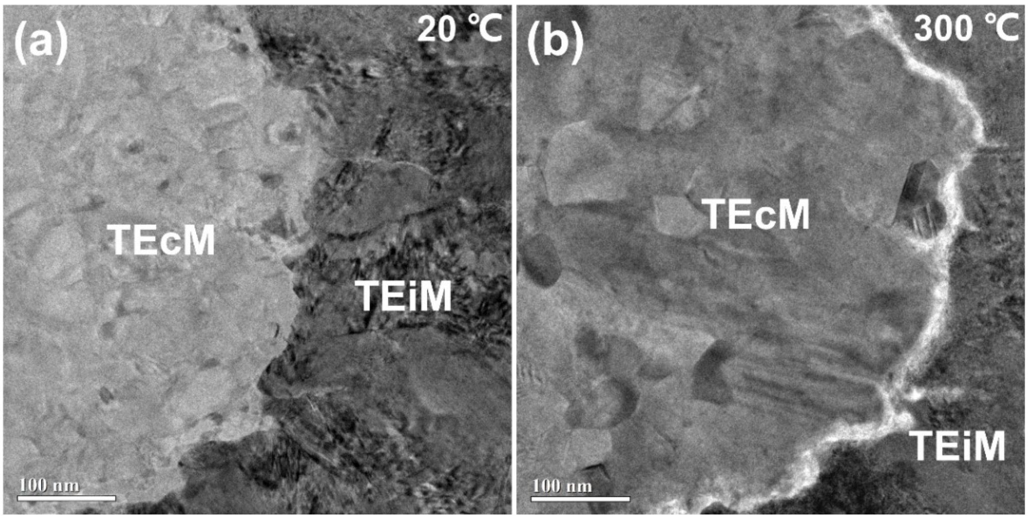

Figure. S 16 in-situ TEM images of the $AgMgMn_{0.1}$/MgAgSb interface under different temperature, (a) 20 and (b) 300 °C.

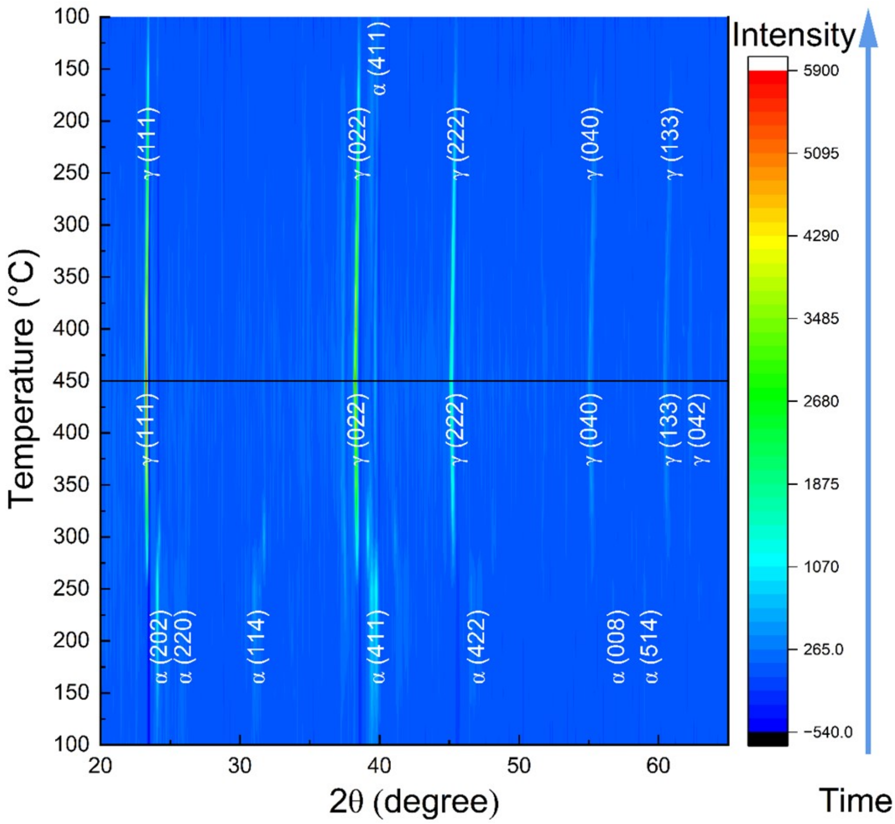

Figure. S 17 In-situ XRD patterns of the MgAgSb bulk heating from 100 to 450 °C then cooling to 100 °C.

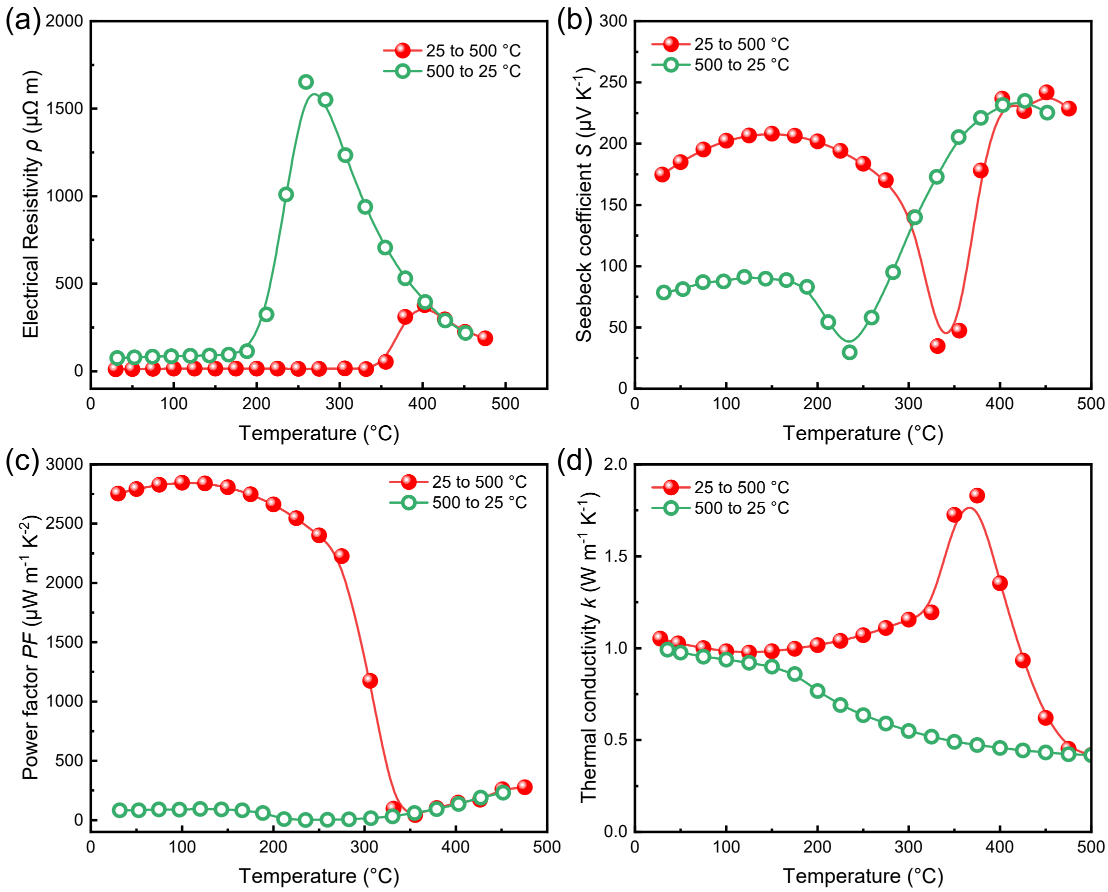

Figure. S 18 The temperature-dependent TE properties of the as-fabricated MgAgSb bulk during the temperature cycle between 25 to 500 °C. (a) Electrical resistivity, (b) Seebeck coefficient, (c) power factor, (d) thermal conductivity.

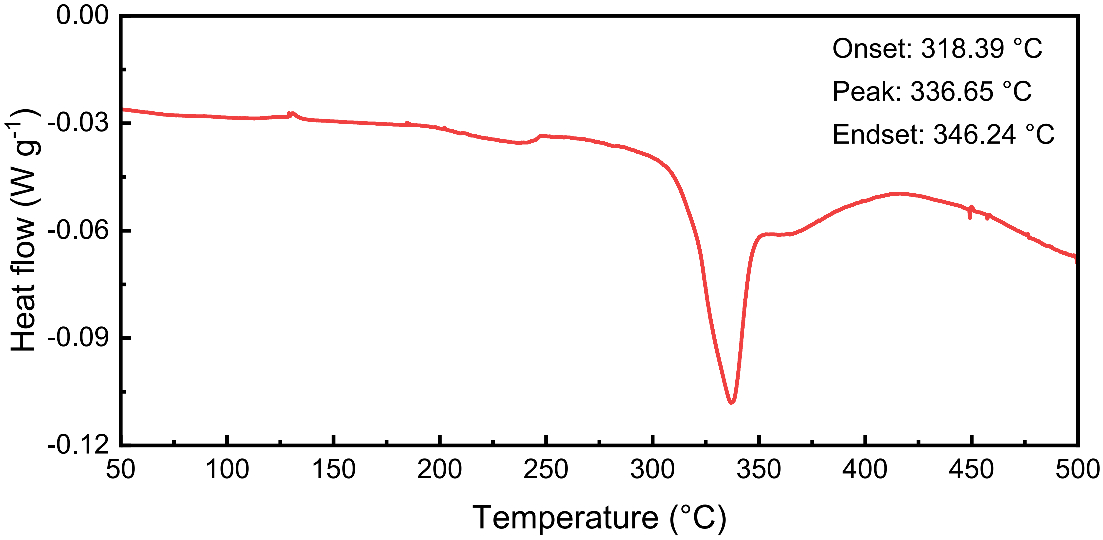

Figure. S 19 Differential Scanning Calorimetry (DSC) curve of MgAgSb

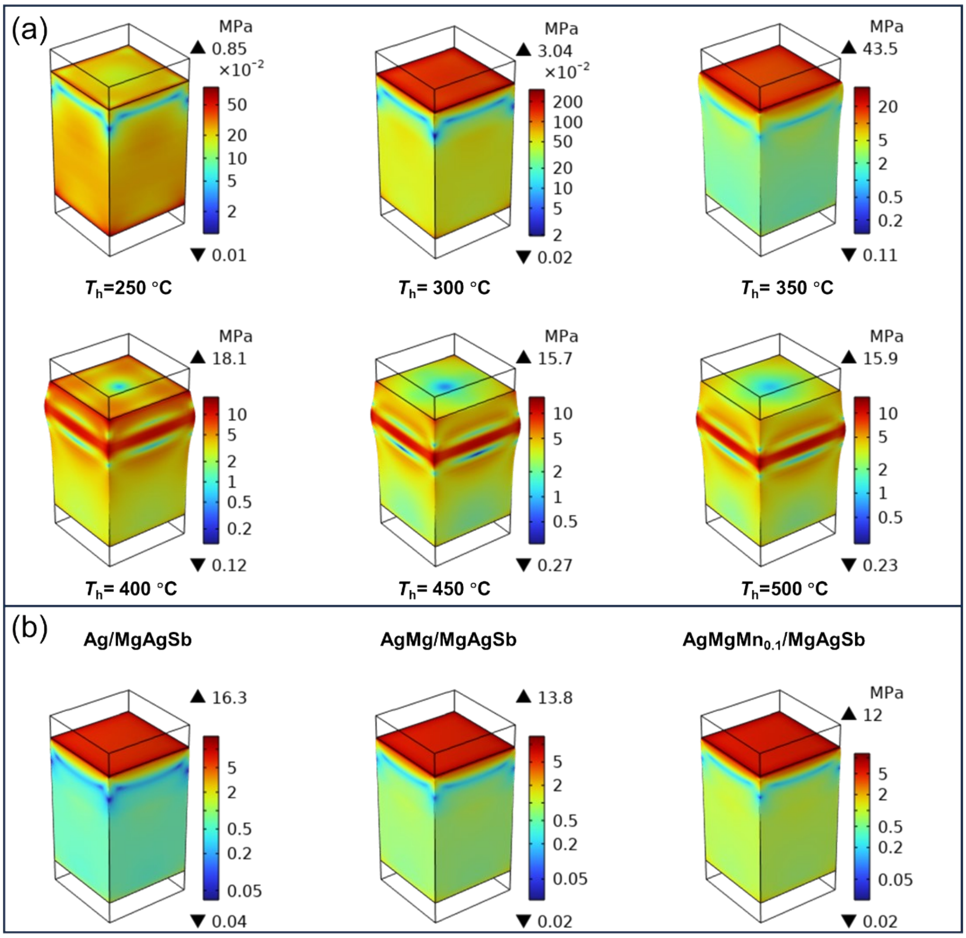

Figure. S 20 Simulated von Mises stress distribution. (a) T_h-dependent von Mises stress distribution of $AgMgMn_{0.1}$/MgAgSb interface (T_c = 5 °C), (b) TEiM/MgAgSb interface under a T_h of 320 °C (TEiM =Ag, AgMg, and $AgMgMn_{0.1}$).

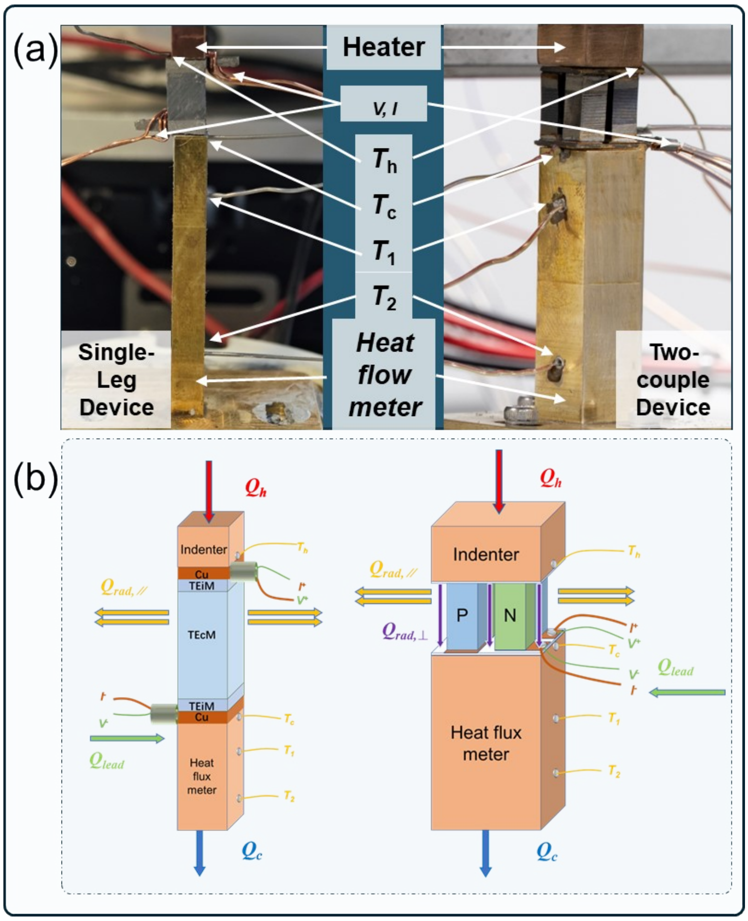

Figure. S 21 Photographs of measurement setup for single-leg and 2-pair module devices, (b) Conceptual diagram on the estimation of Q_h

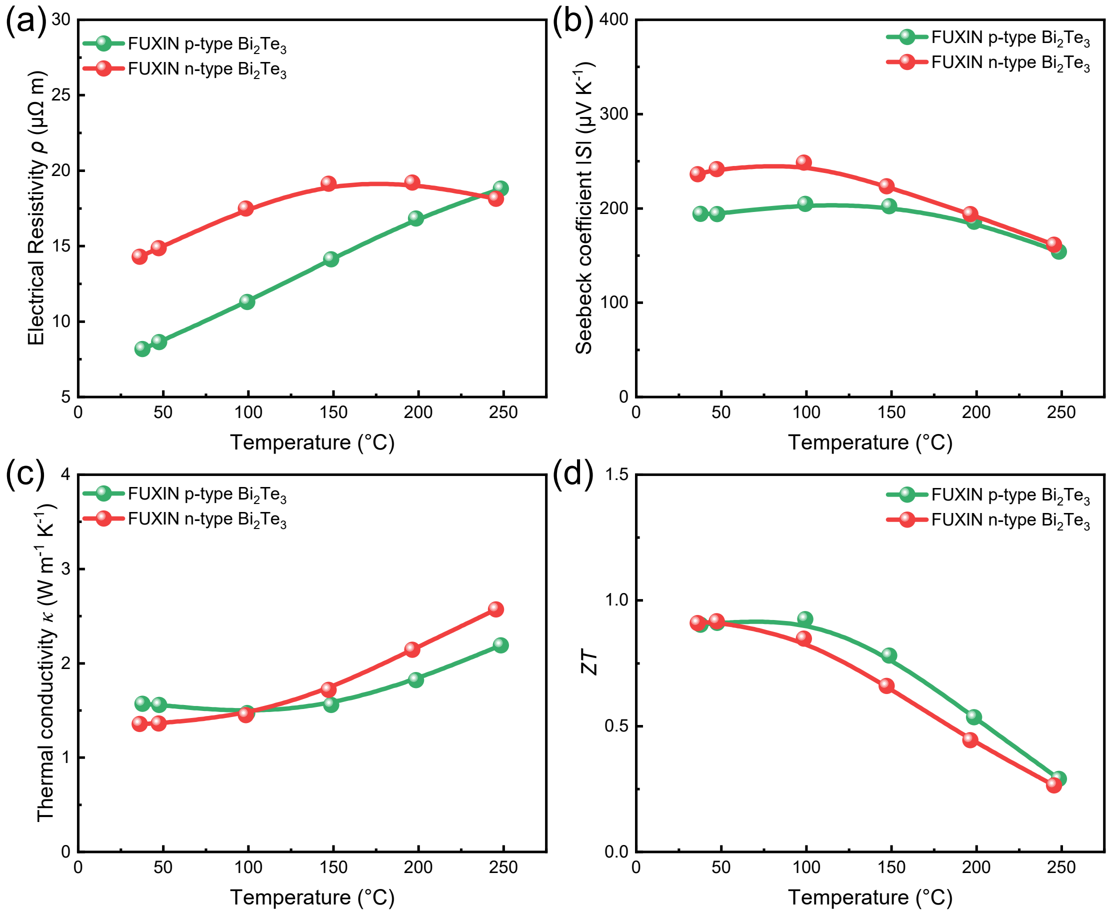

Figure. S 22 Temperature-dependent TE properties of the FUXIN commercial Bi_2Te_3 (a) Electrical resistivity, (b) Seebeck coefficient, (c) thermal conductivity, and (d) *ZT*.

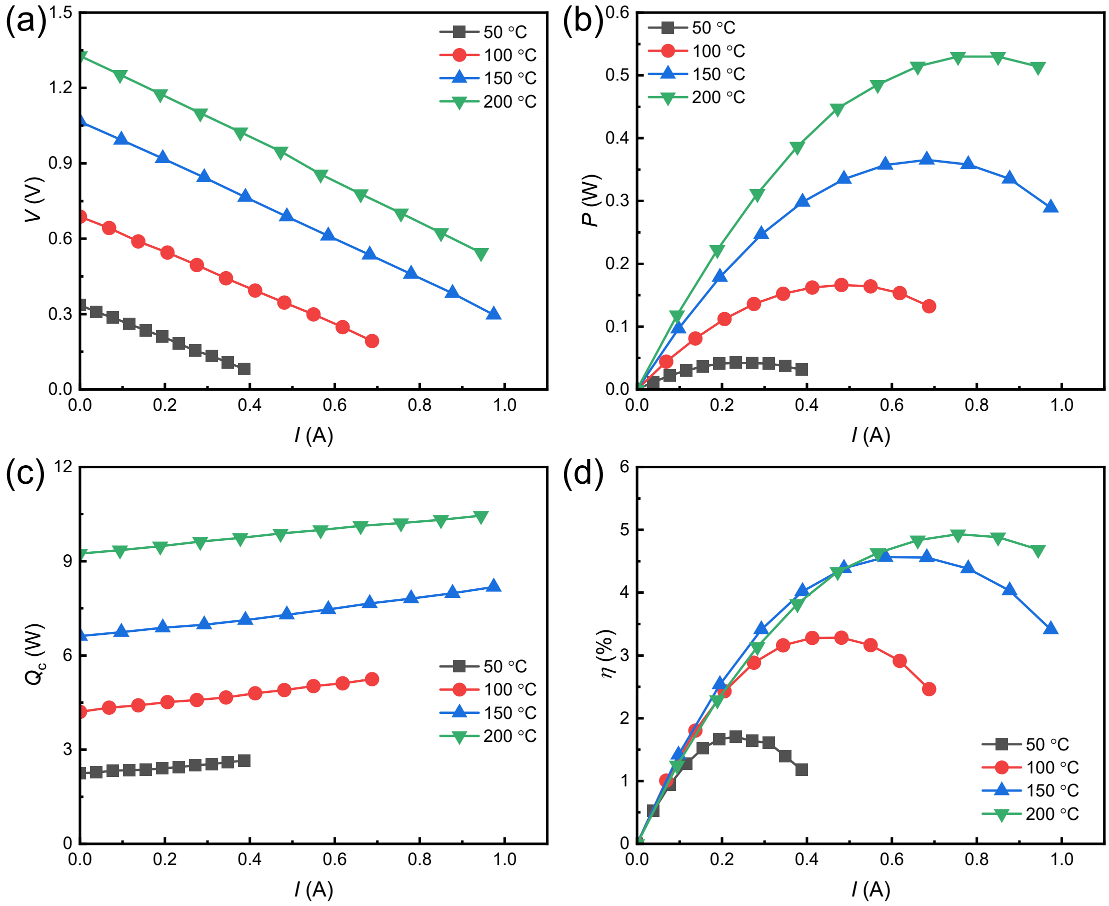

Figure. S 23 Performance of the FUXIN commercial Bi_2Te_3 Module devices under different temperature differences (ΔT). (a) Current I-dependent output voltage V, (b) I-dependent out power P, (c) I-dependent cold side heat flow Q_c, (d) I-dependent conversion efficiency η.

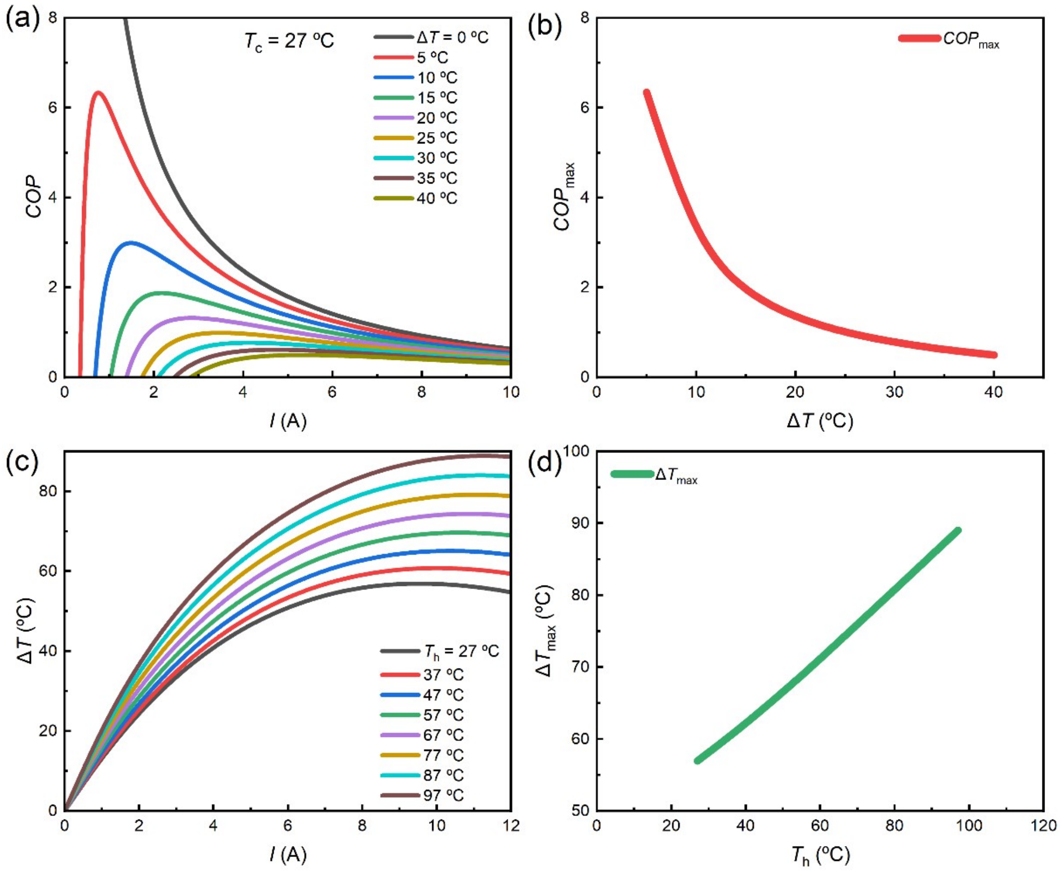

Figure. S 24 Simulated performance of the single leg TEC devices (a) Current *I*-dependent coefficient of performance (COP) under different temperature differences (ΔT), (b) ΔT -dependent COP_{max}, (c) *I*-dependent ΔT under different hot side temperatures (T_h), (d) T_h-dependent ΔT_{max}.

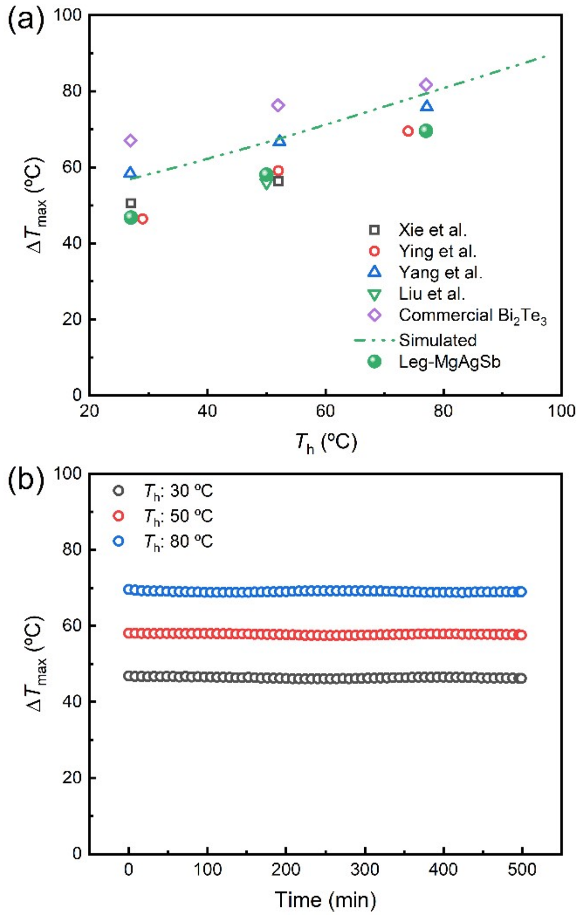

Figure. S 25 Performance and stability of the single leg and two-couple TEC devices (a) T_h-dependent (maximum cooling temperature) ΔT_{max}, (b) the plot of ΔT_{max} vs. in-situ testing time at different T_h in a vacuum. Literature results [11, 13-15] are included for comparison.

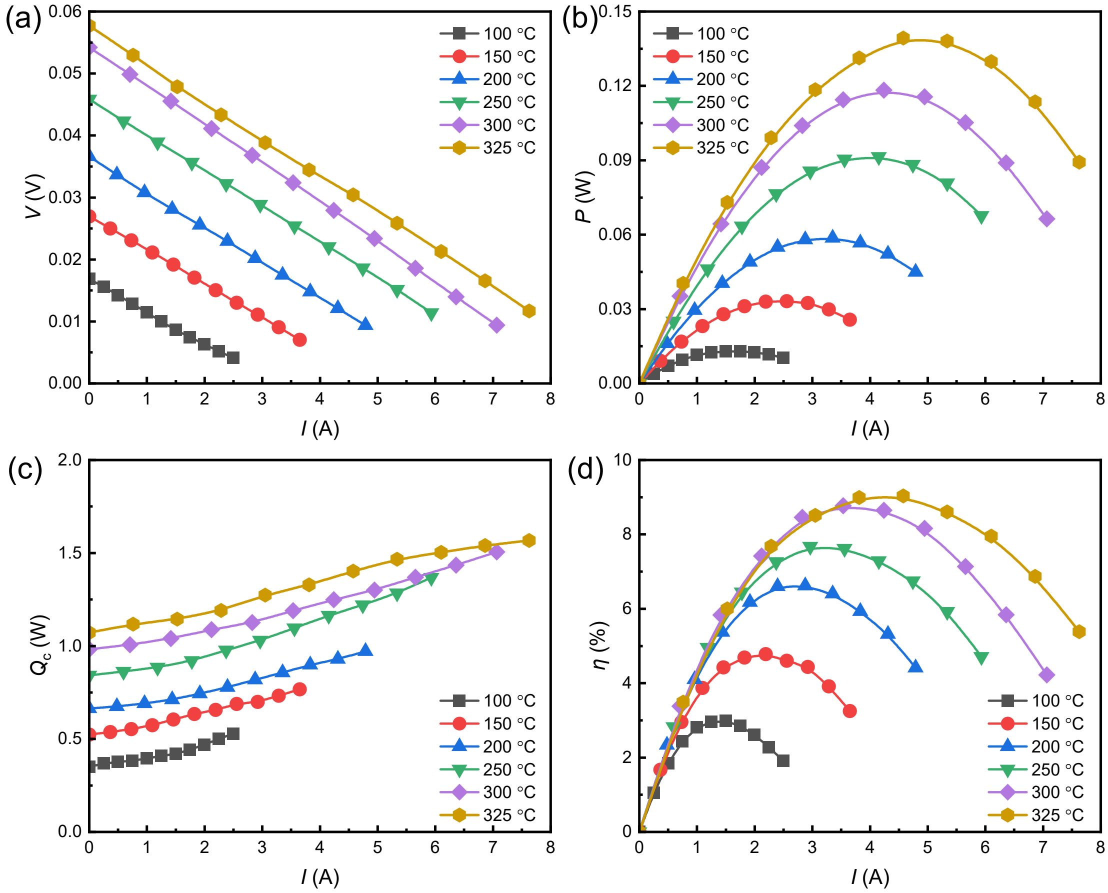

Figure. S 26 Performance of the single leg TEG devices under different temperature differences ΔT. (a) Current I-dependent output voltage V, (b) I-dependent out power P, (c) I-dependent cold side heat flow Q_c, (d) I-dependent conversion efficiency η.

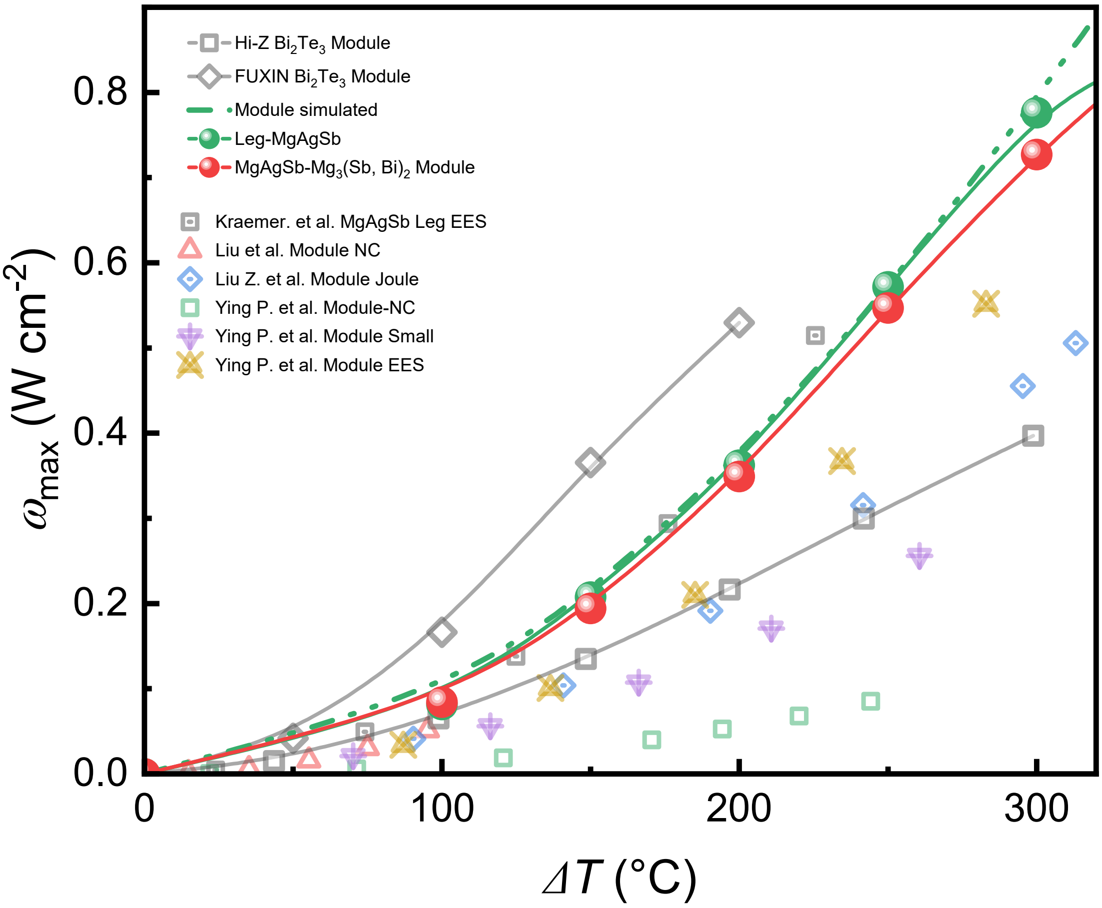

Figure. S 27 ω_{max} of the TEG devices under different temperature differences ΔT, including pertinent literature results [9-13, 16, 17].

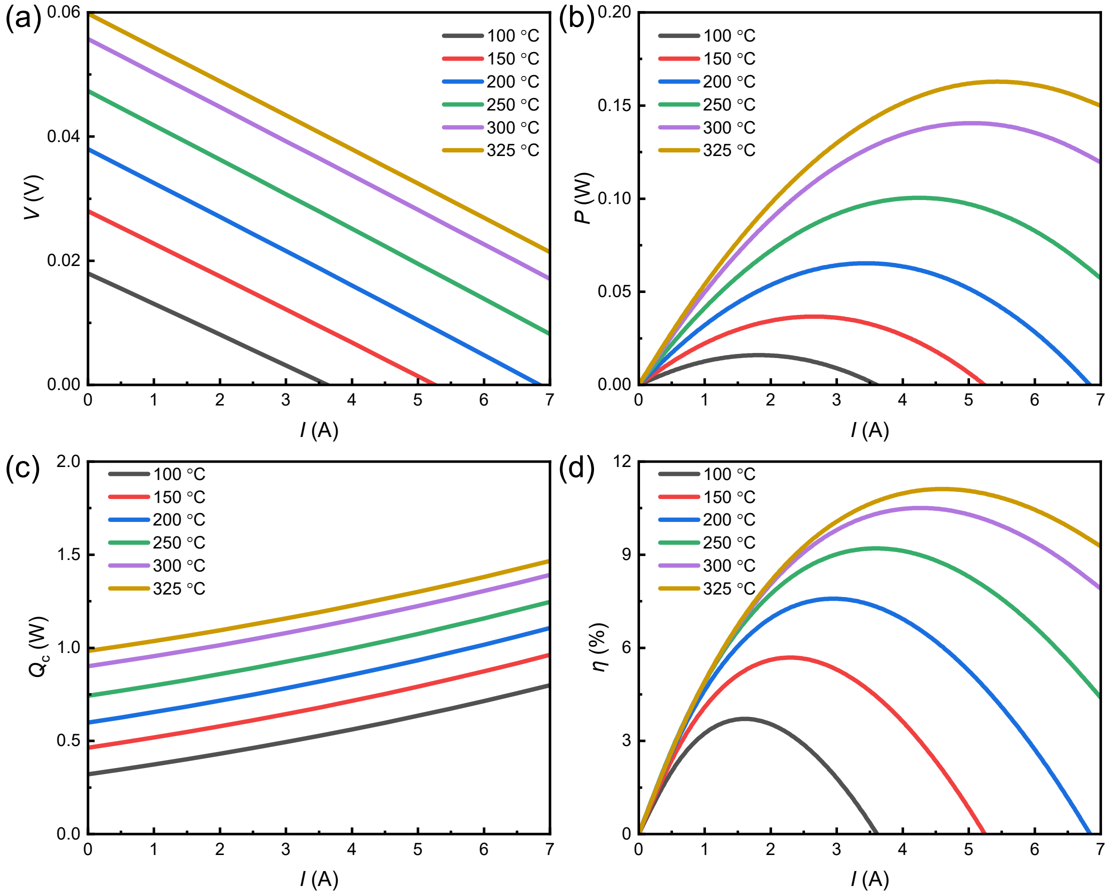

Figure. S 28 Theoretically Simulated performance of the single leg TEG devices under different temperature differences ΔT. (a) Current I-dependent output voltage V, (b) I-dependent out power P, (c) I-dependent cold side heat flow Q_c, (d) I-dependent conversion efficiency η.

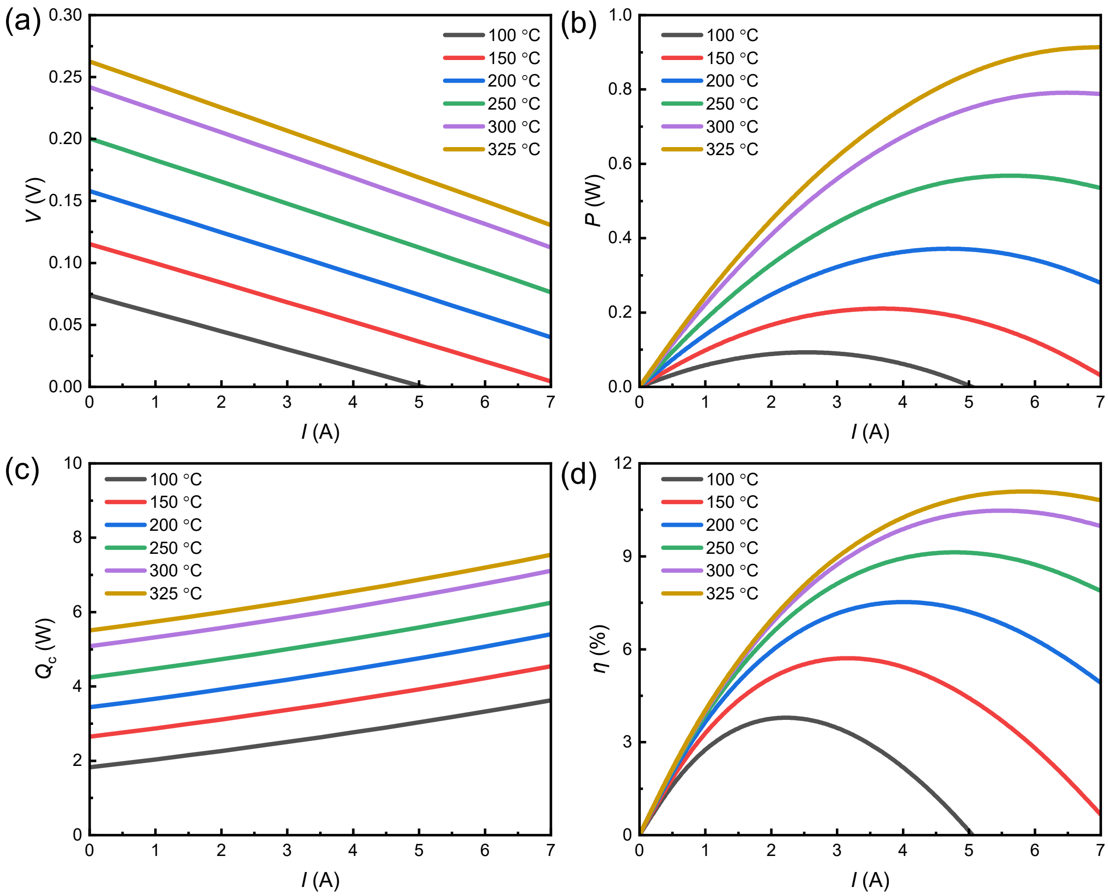

Figure. S 29 Theoretically Simulated performance of the two-couple TEG devices under different temperature differences ΔT. (a) Current I-dependent output voltage V, (b) I-dependent out power P, (c) I-dependent cold side heat flow Q_c, (d) I-dependent conversion efficiency η.

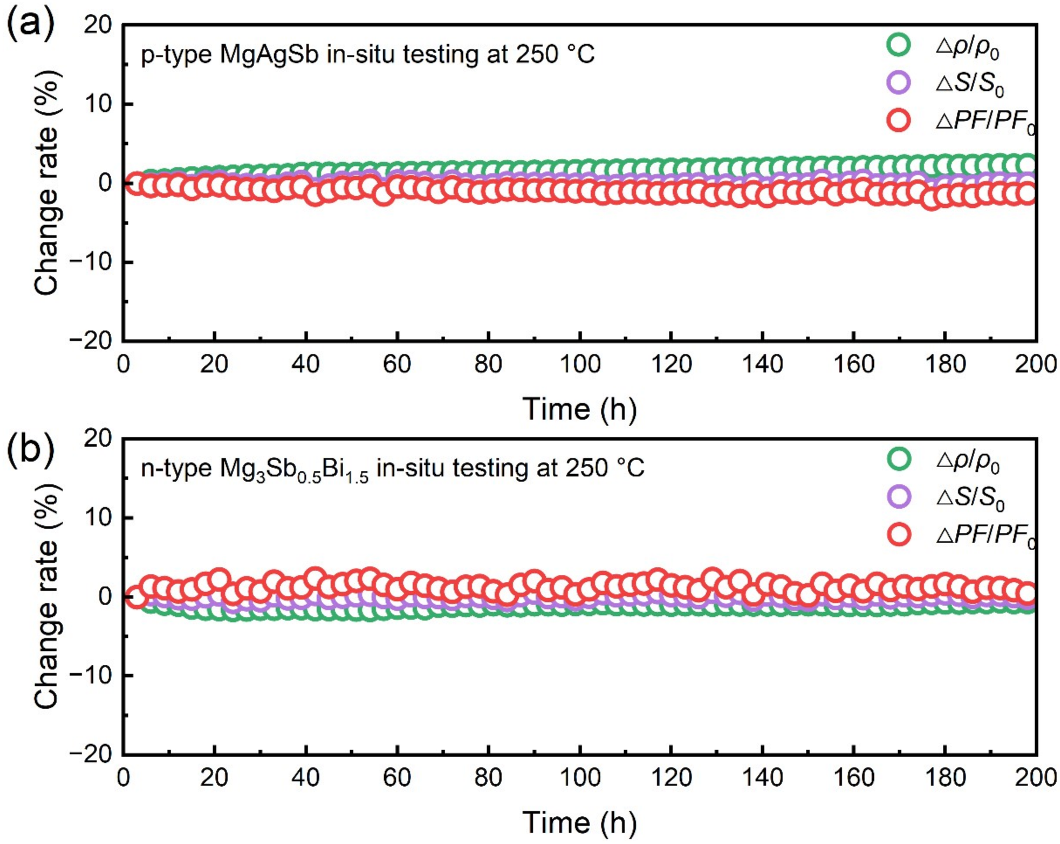

Figure. S 30 Thermal stability of TEcM. Plots of (a) $\Delta\rho/\rho_0$, (b) $\Delta S/S_0$, and (c) $\Delta PF/PF_0$ vs. in situ testing time at 250 °C.

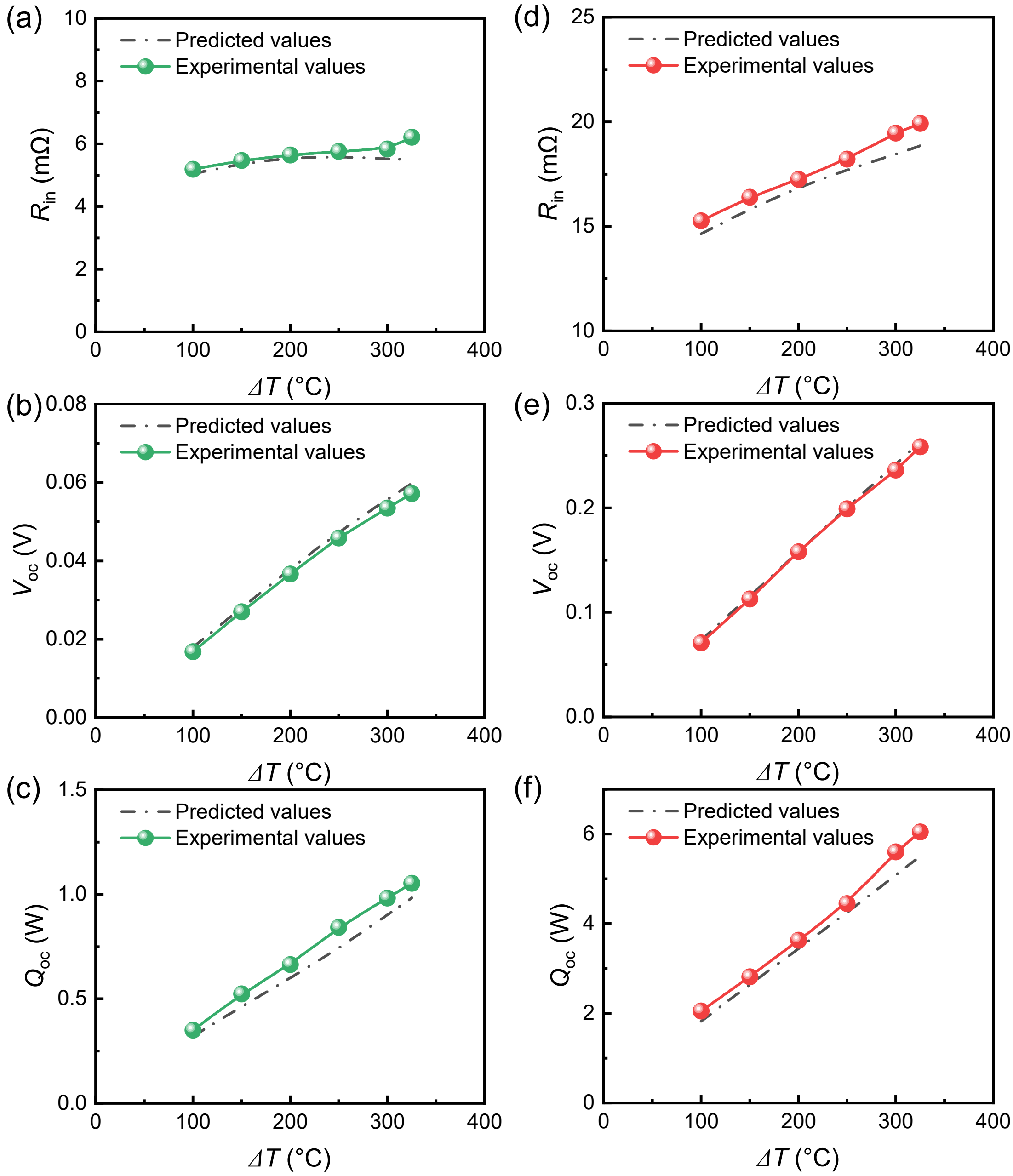

Figure. S 31 Comparison between experimental and theoretical internal resistance, open-circuit voltage, and heat flow of single-leg (a, b, and c) and two-couple module (d, e, and f) devices.

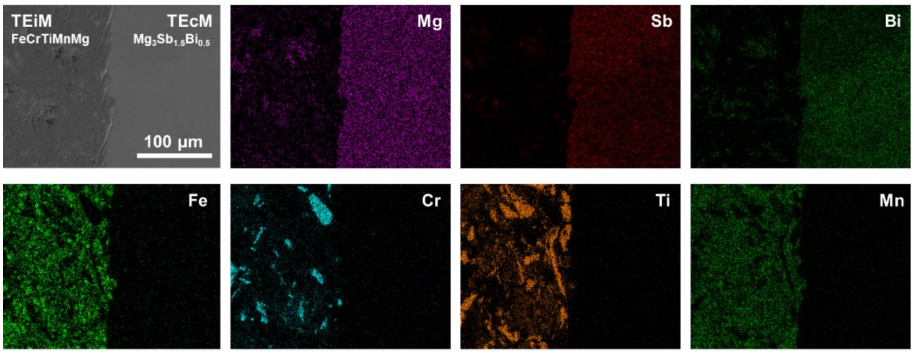

Figure. S 32 SEM and EDS Mapping of the FeCrTiMnMg/$Mg_3Sb_{1.5}Bi_{0.5}$ interfaces.

4. Table. S

Table. S 1 T_m of metals and TEcM (MgAgSb)

Metals/TEcM	T_m (°C)	Metals/TEcM	T_m (°C)
Fe	1538	Al	660
Cu	1083	Mg	650
Ni	1455	Zn	420
Ag	962	Mn	1245
Ti	1668	V	1910
Co	1495	Cr	1855
TEcM	550		

Table. S 2 σ_s and ρ_c of $AgMgMn_{0.1}$/MgAgSb contact interface versus aging treatment time at 250 °C.

Aging Time (Day)	σ_s (MPa)	ρ_c (μΩ cm^2)
0	35.0 ±8.8	4.5 ±1.4
1	35.5 ±9.2	4.4 ±2.5
3	33.9 ±7.5	5.1 ±1.7
7	33.8 ±6.3	5.7 ±2.8
15	33.1 ±9.5	5.2 ±2.6

Table. S 3 Estimation of lead heat leakage and thermal radiation for single-leg device.

ΔT (°C)	Q_{lead} (mW)	Q_c (mW)	$Q_{rad,\perp}$ (mW)	$Q_{rad,//}$ (mW)	η (%)	η_{cali} (%)
100	19.9	349.9	0.0	4.3	3.0	2.9
150	20.2	523.9	0.0	10.5	4.8	4.7
200	20.2	664.0	0.0	20.8	6.6	6.4
250	19.9	841.6	0.0	38.6	7.7	7.5
300	19.9	982.4	0.0	52.9	9.0	8.5
325	19.8	1053.3	0.0	71.6	9.1	8.4

Table. S 4 Estimation of lead heat leakage and thermal radiation for two-couple module device.

ΔT (°C)	Q_{lead} (mW)	Q_{c} (mW)	$Q_{\mathrm{rad},\perp}$ (mW)	$Q_{\mathrm{rad},//}$ (mW)	η (%)	η_{cal} (%)
100	19.8	2053.2	10.0	25.0	3.3	3.2
150	19.9	2813.6	22.5	56.2	5.3	5.3
200	20.0	3634.6	45.6	114.0	7.3	7.2
250	20.1	4451.2	81.6	204.1	8.6	8.4
300	19.9	5601.8	127.4	318.6	9.3	9.0
325	19.9	6046.4	164.4	410.9	9.4	9.1

References

[1] Y. Y. Zheng, C. Y. Liu, L. Miao, C. Li, R. Huang, J. Gao, X. Y. Wang, J. L. Chen, Y. C. Zhou, E. Nishibori, *Nano Energy* **2019**, *59*, 311.

[2] F. Jiang, T. Feng, Y. Zhu, Z. Han, R. Shu, C. Chen, Y. Zhang, C. Xia, X. Wu, H. Yu, C. Liu, Y. Chen, W. Liu, *Mater. Today Phys.* **2022**, *27*, 100835.

[3] X. Wu, Z. Han, Y. Zhu, B. Deng, K. Zhu, C. Liu, F. Jiang, W. Liu, *Acta Mater.* **2022**, *226*, 117616.

[4] X. Wu, Y. Lin, Z. Han, H. Li, C. Liu, Y. Wang, P. Zhang, K. Zhu, F. Jiang, J. Huang, H. Fan, F. Cheng, B. Ge, W. Liu, *Adv. Energy Mater.* **2022**, *12*, 2203039.

[5] Z. Bu, X. Zhang, Y. Hu, Z. Chen, S. Lin, W. Li, C. Xiao, Y. Pei, *Nat. Commun.* **2022**, *13*, 237.

[6] C. Xu, Z. Liang, W. Ren, S. Song, F. Zhang, Z. Ren, *Adv. Energy Mater.* **2022**, *12*, 2202392.

[7] L. Yin, F. Yang, X. Bao, W. Xue, Z. Du, X. Wang, J. Cheng, H. Ji, J. Sui, X. Liu, Y. Wang, F. Cao, J. Mao, M. Li, Z. Ren, Q. Zhang, *Nat. Energy* **2023**, *8*, 665.

[8] Z. Liang, C. C. Xu, H. Shang, Q. Zhu, F. Z. Ding, J. Mao, Z. F. Ren, *Mater. Today Phys.* **2021**, *19*, 100413.

[9] D. Kraemer, J. Sui, K. McEnaney, H. Zhao, Q. Jie, Z. F. Ren, G. Chen, *Energ Environ. Sci.* **2015**, *8*, 1299.

[10] P. J. Ying, R. He, J. Mao, Q. Zhang, H. Reith, J. H. Sui, Z. F. Ren, K. Nielsch, G. Schierning, *Nat. Commun.* **2021**, *12*, 1121.

[11] Z. Liu, W. Gao, H. Oshima, K. Nagase, C. H. Lee, T. Mori, *Nat. Commun.* **2022**, *13*, 1120.

[12] Z. H. Liu, N. Sato, W. H. Gao, K. Yubuta, N. Kawamoto, M. Mitome, K. Kurashima, Y. Owada, K. Nagase, C.-H. Lee, J. H. Yi, K. Tsuchiya, T. Mori, *Joule* **2021**, *5*, 1196.

[13] P. Ying, L. Wilkens, H. Reith, N. P. Rodriguez, X. Hong, Q. Lu, C. Hess, K. Nielsch, R. He, *Energ Environ. Sci.* **2022**, *15*, 2557.

[14] L. Xie, J. Yang, Z. Liu, N. Qu, X. Dong, J. Zhu, W. Shi, H. Wu, G. Peng, F. Guo, Y. Zhang, W. Cai, H. Wu, H. Zhu, H. Zhao, Z. Liu, J. Sui, *Materials Today* **2023**, *65*, 5.

[15] J. Mao, Z. H. Liu, Z. F. Ren, *Science* **2019**, *365*, 495.

[16] P. Ying, H. Reith, K. Nielsch, R. He, *Small* **2022**, *18*, e2201183.

[17] L. Xie, L. Yin, Y. Yu, G. Peng, S. Song, P. Ying, S. Cai, Y. Sun, W. Shi, H. Wu, N. Qu, F. Guo, W. Cai, H. Wu, Q. Zhang, K. Nielsch, Z. Ren, Z. Liu, J. Sui, *Science* **2023**, *382*, 921.